J Mater Sci (2008) 43:1612–1618
DOI 10.1007/s10853-007-2333-z

Measurement and analytical validation of interfacial bond strength of PAN-fiber-reinforced carbon matrix composites

Jale Tezcan · Soydan Ozcan · Bijay Gurung · Peter Filip

Received: 6 July 2007 / Accepted: 19 November 2007 / Published online: 25 December 2007

Abstract Carbon/carbon composites are well suited to high-friction applications due to their excellent mechanical and thermal properties. Since interfacial shear strength is critical to composite performance, characterization of fiber/matrix interface is a crucial step in tailored design of composites. This article presents a hybrid experimental/analytical study to evaluate the interfacial shear strength (IFSS) of PAN-fiber-reinforced carbon matrix composites. Microstructure was studied by light and high-resolution transmission electron microscopy (HRTEM). A series of push-out tests were conducted to examine the fiber/matrix debonding process. The residual fiber displacement was confirmed by scanning electron microcopy (SEM). The validity of the calculated IFSS value was demonstrated by a simplified analytical approach, where the components contributing to the measured displacement were analyzed considering the mechanics of the indentation. The method described in this article has been successfully used for determining the IFSS of PAN-fiber-reinforced carbon matrix composites.

J. Tezcan (✉)
Civil and Environmental Engineering, Southern Illinois University, Carbondale, IL, USA
e-mail: tezcan@engr.siu.edu

S. Ozcan · B. Gurung · P. Filip
Mechanical Engineering and Energy Processes, Southern Illinois University, Carbondale, IL, USA

S. Ozcan · B. Gurung · P. Filip
Center for Advanced Friction Studies, Southern Illinois University, Carbondale, IL, USA

Introduction

PAN-fiber-reinforced carbon matrix composites (C/C) are often used in braking applications because of their low density, high specific heat and thermal conductivity, as well as their unique capacity to retain high strength, toughness, and thermal properties at elevated temperatures [1–3].

It has been shown that the mechanical properties of the composites are greatly affected by fiber/matrix interface [4–8], fiber architecture [9], and the intrinsic nature of the fiber and the matrix [10–12]. The fiber/matrix interface serves as a buffer for stresses acting on the bulk composite when microcracking occurs upon loading. Since the reinforcing fibers bridge the matrix cracks, the fiber/matrix interface is critical in directing the cracks in the composite. Strength and stiffness of composite typically increases with higher IFSS, however, at the expense of fracture toughness [13]. A weak fiber/matrix interface tends to promote fracture toughness by redirecting the microcracks to the interface. However, too weak an interface is not suitable for applications when oxidative effects are important [14, 15].

The main purpose of this article is to present a hybrid experimental/analytical study to evaluate the IFSS of PAN-fiber-reinforced carbon matrix composites. Microstructure was studied by polarized light microscopy (PLM) and high-resolution transmission electron microscopy (HRTEM). A total of 60 single fiber push-out tests were conducted to study the fiber/matrix debonding process. The residual fiber displacement was confirmed by scanning electron microcopy (SEM). The push-out data from the indentation experiments were used to calculate the IFSS and a simple analytical procedure was developed to demonstrate the validity of the results.

Experimental

The C/C composite used in this research is the commercially available aircraft brake material CARBENIX® 4000 series manufactured by Honeywell International. The composite consists of chemical vapor infiltrated (CVI) carbon matrix and three-directional non-woven PAN-based carbon fibers.

Microstructure of the composite was characterized using a Nikon Eclipse LV150 polarized light microscope (PLM). Inspected areas were perpendicular to the friction surface of the brake discs. C/C samples were mounted in epoxy resin ground and polished (SiC paper ranging from 180 to 1,200 grit) using diamond polishing slurries with grain sizes from 6 down to 0.25 μm.

High-resolution transmission electron microscopy studies were carried out using Hitachi 7650 and JEOL 2010EF transmission electron microscopes at accelerating voltages of 100 and 200 kV, respectively. The HRTEM samples were prepared using a linear precision diamond saw (Buehler, Isomet 4000), core-drill (VCR Group, Model V 7110), dimpler (D 500, VCR Group Inc., CA), and the Precision Ion Polishing System (Gatan, 691). The final thinning of samples to thickness ~100 nm was performed with the polishing stage set at 4° angle at 3 keV.

Specimens, with dimensions approximately 15 × 15 × 15 mm, were randomly cut from different discs to be used in both the nanoindentation and the PLM studies. After being mounted into an epoxy resin, the specimens were polished using diamond slurries with a grain-size ranging from 6 down to 0.25 μm. The polishing was completed with a 0.05 μm grain size alumina suspension. The moduli of elasticity of the fiber and the matrix were measured at room temperature using a Nano Indenter® XP system (MTS Nanoinstruments, Knoxville, TN) with a Berkovich-type diamond tip. Fused silica was used to calibrate the system before each test. The maximum indenter displacement was 300 nm with a drift rate lower than 0.05 nm/s. Microscope to indenter calibration has been performed prior to each series of measurements by making five indents on fused silica, placing the cursor in the middle of the center indent. By this way, the indent location can be determined with a precision of ± 0.25 μm along the x and y directions. After each test, the location of indent was inspected using light microscope.

The moduli of elasticity were determined using the continuous stiffness measurement [16, 17]. Thirty indents in 30 randomly selected fibers were performed, and the matrix was also indented at 30 randomly selected locations. The moduli of elasticity were found to be 18.20 (±2.2) and 17.80 (±1.8) MPa for fiber and matrix, respectively.

For push-out testing, three thin specimens (~500 μm thick) perpendicular to the friction surface of the brake discs were cut using a diamond saw (Buehler, Isomet 4000). Samples were pre-thinned using SiC abrasive paper and polished to a thickness of 200 μm using Buehler Minimet 1000 (Model No. 69-1100) with micro-cloth containing 0.05 μm Al_2O_3 slurry. The 200 (± 2.3)-μm thick C/C specimens were mounted on a 3 mm TEM copper grid using a crystal bond wax to form a beam and placed on a specimen holder as shown in Fig. 1.

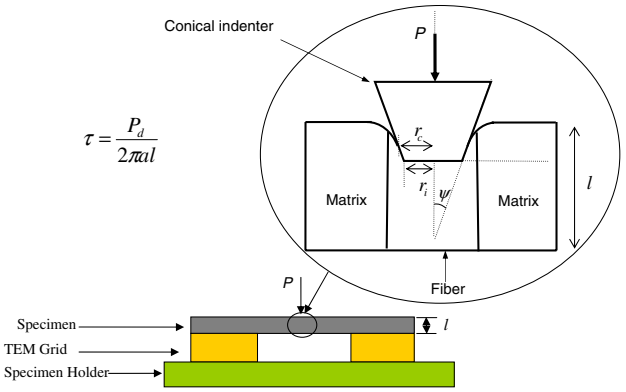

Fig. 1 Schematic of specimen setup and deformation during the push-out test in the nanoindenter

A total of 60 push-out tests were conducted on three specimens. Before testing, the surface of each specimen was inspected by the nanoindenter's light microscope to select the fibers with perpendicular orientation. All push-out tests were conducted at room temperature, using a Nano Indenter® (XP system, MTS Nanoinstruments, Knoxville, TN), using a 60° cone indenter with 5-μm diameter flat-end tip. A constant load rate of 0.66 mN/s was applied until the preset maximum load of 108 mN was reached. The surfaces of the specimens were inspected after the tests to confirm fiber push-out and to detect any fracturing in the fiber or matrix.

Results and discussion

Microstructure

The typical microstructure of the investigated C/C composite obtained by a polarized light microscope (PLM) is shown in Fig. 2. PAN-fibers with turbostratic microstructure and diameter ranging between 6 and 9 μm are surrounded by a rough laminar CVI carbon. While rotating the polarizer of the PLM, the CVI-matrix displayed contrast with an average extinction angle Ae = 20°, indicating the presence of rough laminar microstructure. As a consequence of gas transport limitations, the deposition thickness of CVI carbon is large in the vicinity of large pores and it is much smaller within the carbon fiber bundle regions. Larger microporosity formed

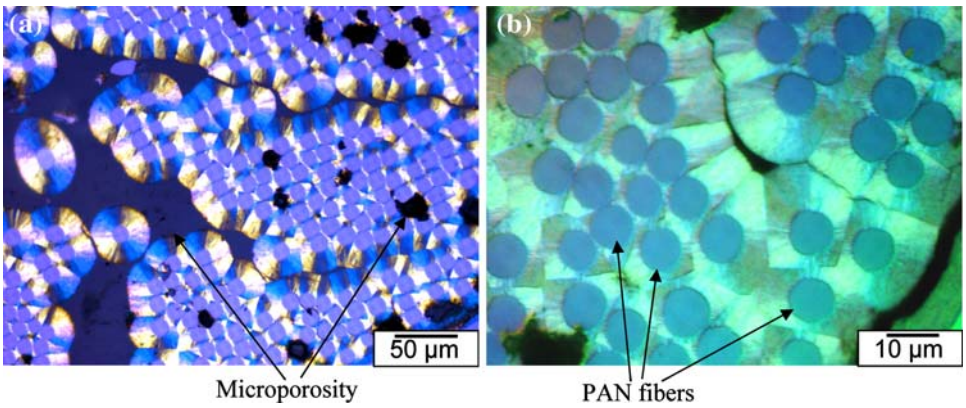

Fig. 2 Low (**a**) and high (**b**) magnification PLM photomicrographs of investigated C/C composite (PLM)

dominantly between the fiber bundles (Fig. 2a), whereas the interior surfaces of the fiber bundles were typified by smaller pores (Fig. 2b).

Low- and high-magnification micrographs of fiber, matrix, and interface as observed in HRTEM are shown in Fig. 3. The fiber/matrix interface often contains microcracks separating the carbon fiber from the surrounding CVI-matrix (marked by arrows in Fig. 3a). Whether these microcracks are formed during the HRTEM sample preparation stage is not clear. However, careful inspection of the intact parts in the fiber/matrix interface revealed the presence of two types of microstructure: (i) well-developed amorphous interface (Fig. 3b), and (ii) fiber in direct contact with the CVI-matrix (Fig. 3c). The PAN-based carbon fiber exhibits the typical turbostratic microstructure as seen in Figs. 3b and c. The graphene sheets visible in CVI-matrix are weakly ordered and aligned randomly with respect to the fiber/matrix interface. The observed

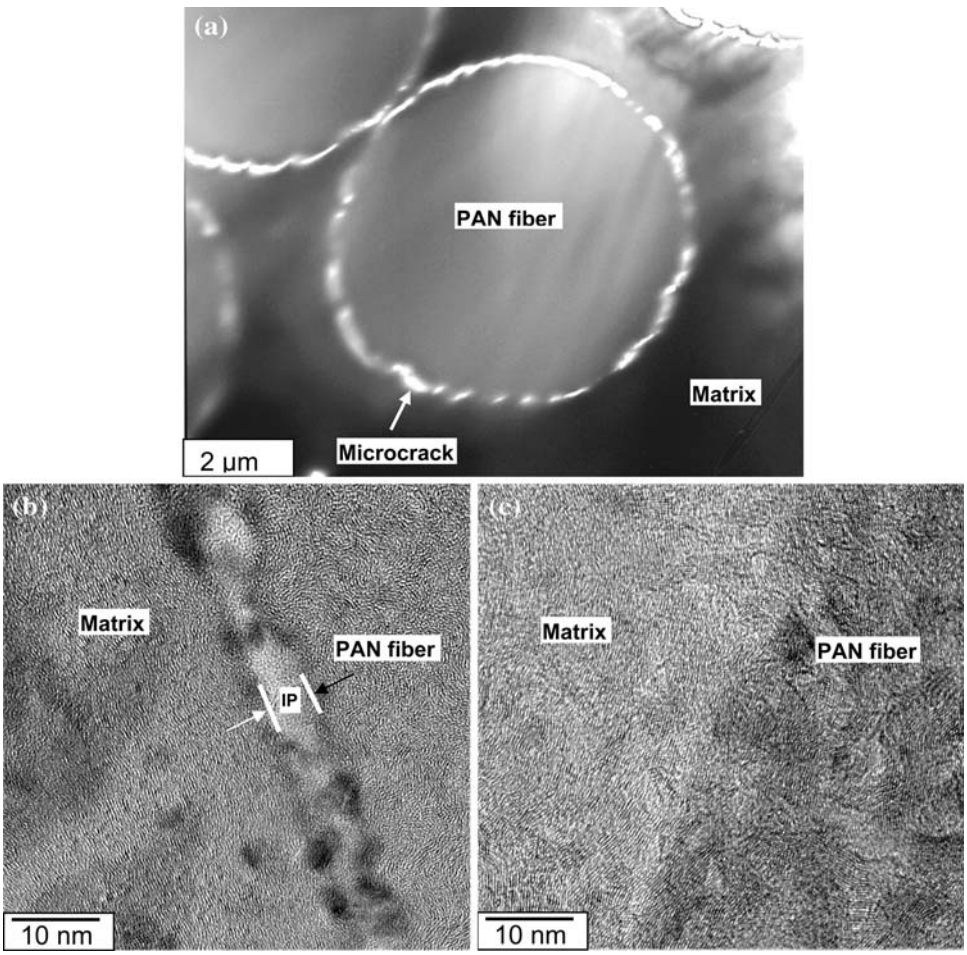

Fig. 3 Low (**a**) and high (**b**, **c**) magnification HRTEM images of the fiber/matrix interface

similarity in the microstructure of fiber and matrix explains the closeness of the two modulus of elasticity values.

Interfacial shear strength measurements

Figure 4 shows the characteristic load versus displacement behavior observed in push-out tests. The initial semi-linear part of load–displacement graph is followed by a highly non-linear section. The non-linearity is caused by combination of elastic deformation of fiber and matrix, elastic bending of the entire specimen, and possible irreversible shear processes in the CVI-matrix having a better developed graphite-like structure [18]. The plateau observed between points B and C in Fig. 4 represents the sudden failure on the fiber/matrix interface. The sudden debonding with initial crack formation is attributed to the fiber length being shorter than the critical length [19]. The load increase observed after point C (Fig. 4) is explained by the formation of the contact between the conical indenter and the CVI-matrix after the tip pushes out the fiber. SEM micrographs in Figs. 5b, c clearly display the complete fiber/matrix debonding. No evidence of fiber indentation, fiber cracking, or matrix cracking was found. Analysis of experimental data revealed that the average load at the plateau (Fig. 4) was 80.7 ± 9.1 mN. Assuming uniform shear stress distribution throughout the fiber/matrix interface, and ignoring the effects of radial stresses, the interfacial shear strength (IFSS) is calculated as

$$\tau = \frac{P_d}{2\pi a l} = 14.3 \pm 2.3\,\text{MPa} \quad (1)$$

In Eq. 1, a and l are the radius of fiber and thickness of the specimen, respectively. The standard deviation of the IFSS was estimated using the square roots of sum of the squares of the standard deviations of the P_d, a, and l measurements.

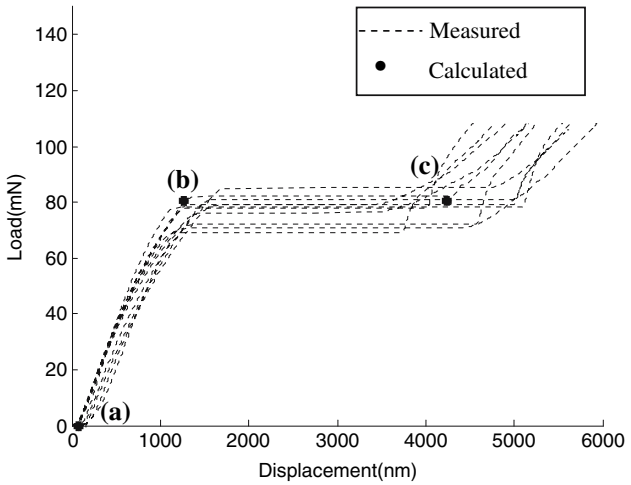

Fig. 4 Load–displacement measurements and analytical estimates

Analytical validation of the test results

This section describes an inverse approach to obtain the critical points on the load–displacement curve using the mechanical properties of the tested specimen. The measured displacement can be written as a summation of four components

$$u = u_{ep} + u_c + u_s + u_b \quad (2)$$

where u_{ep} is the penetration of the indenter into the fiber; u_c is the elastic deformation of the fiber under compression; u_s is the sliding displacement of the debonded fiber relative to the matrix; and u_b is the bending deflection of the entire specimen.

The penetration depth (u_{ep}) is the elastoplastic displacement of the indenter tip relative to surface of the fiber. For an indenter with tip radius (r_i) and included half angle (ψ) (see Fig. 1), the penetration depth (u_{ep}) and the corresponding load (P), are related to the contact radius (r_c) through the equations [20]:

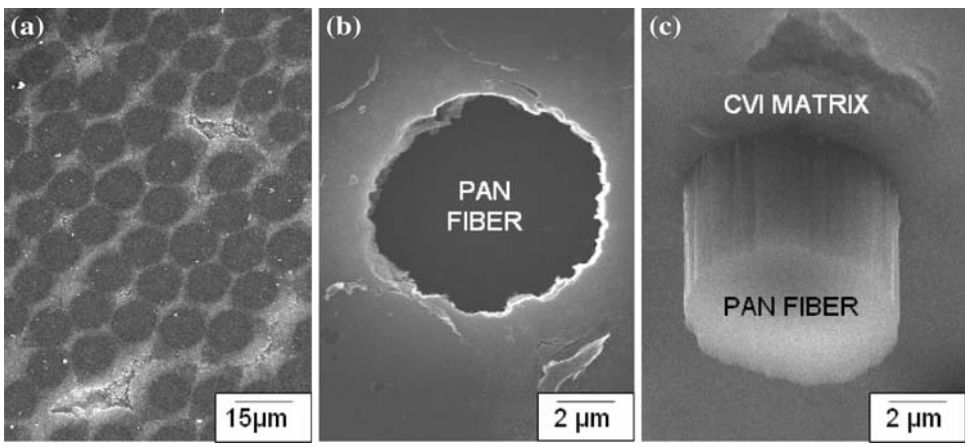

Fig. 5 SEM micrograph of polished surface before push-out (**a**) after the push-out test (**b**) the top of the specimen and (**c**) the bottom of specimen

$$P = \frac{2E_{\text{eff}}}{\tan(\psi)}\left(u_{\text{ep}}\, r_{\text{c}} \tan(\psi) - r_{\text{c}}^2\left[\frac{\pi}{2} - \arcsin\left(\frac{r_{\text{i}}}{r_{\text{c}}}\right)\right] + \frac{b}{a}\sqrt{r_{\text{c}}^2 - r_{\text{i}}^2}\right) \quad (3)$$

$$u_{\text{ep}} \tan(\psi) - r_{\text{c}}\left[\frac{\pi}{2} - \arcsin\left(\frac{r_{\text{i}}}{r_{\text{c}}}\right)\right] = 0 \quad (4)$$

In Eq. 3, a and b are the radii of fiber and matrix, respectively, and E_{eff} is the effective elastic modulus given by:

$$\frac{1}{E_{\text{eff}}} = \frac{(1-\upsilon_{\text{i}}^2)}{E_{\text{i}}} + \frac{(1-\upsilon_{\text{s}}^2)}{E_{\text{s}}} \quad (5)$$

where E_{i}, υ_{i} and E_{s}, υ_{s} are the elastic moduli and Poisson's ratios of the indenter and the specimen, respectively. The elastic compression component during loading can be calculated by a shear lag approach [21]:

$$u_{\text{c}} = \frac{\sigma}{nE_{\text{f}}} \quad (6)$$

where σ is the normal stress at the fiber surface and n is a global stiffness constant that takes into account the elastic properties as well as the environment of the fiber. For a composite with fiber radius (a), and volume fraction of fiber and matrix (V_{f}, V_{m}), the global stiffness constant is given by [22].

$$n = \sqrt{\frac{2}{a^2 E_{\text{m}} E_{\text{f}}}\left[\frac{E_{\text{f}}V_{\text{f}} + E_{\text{m}}V_{\text{m}}}{\frac{V_{\text{m}}}{4G_{\text{f}}} + \frac{1}{2G_{\text{m}}}\left(\frac{1}{V_{\text{m}}}\right)\ln\left(\frac{1}{V_{\text{f}}}\right) - 1 - \frac{V_{\text{f}}}{2}}\right]} \quad (7)$$

where E_{f}, G_{f} and E_{m}, G_{m} are the elastic and shear moduli of fiber and matrix, respectively.

Due to the configuration of the experimental setup, bending stresses are created during loading. The effect of specimen bending on the experimental data depends on the geometry and the mechanical properties of the tested specimen. Experimental findings suggest that for specimens supported on grids that are two times wider than the specimen thickness, bending induced effects should not be ignored [23].

An "exact" analysis of bending deformations normally requires three-dimensional stress analysis. However, for most practical applications, the small-deflection theory of plates leads to the solution of bending deformations with sufficient accuracy [24]. When the bending behavior of a sample is similar to that of a thin, initially flat plate of constant thickness, the bending deformation at any point on the sample can be explicitly determined from a fourth order differential equation, without performing a three-dimensional stress analysis. Specifically, the small-deflection theory accurately estimates the bending behavior when the deflection is less than about half the thickness of the sample. For an L_{x} by L_{y} grid, the deflection of entire sample under the load, when the load is applied at point (x and y) can be approximated by the double series solution [25]:

$$u_{\text{b}}(x,y) = \frac{4P}{\pi^4 D L_{\text{x}} L_{\text{y}}}\sum_{m=1}^{\infty}\sum_{n=1}^{\infty}\left(\frac{\sin\left(\frac{m\pi x}{L_{\text{x}}}\right)\sin\left(\frac{n\pi y}{L_{\text{y}}}\right)}{\left(\frac{m}{L_{\text{x}}}\right)^2 + \left(\frac{n}{L_{\text{y}}}\right)^2}\right)^2, \quad (8)$$

where D is the bending rigidity of the plate given by:

$$D = \frac{El^3}{12(1-\upsilon^2)}. \quad (9)$$

In Eq. 9, l and υ are the thickness and the Poisson's ratio of the specimen, respectively, and E is the modulus of elasticity of the sample.

Since the total displacement measured by the indenter is very small compared to half of the composite thickness (100 μm), the small-deflection theory can be used in the bending analysis of the specimens used in this research. The modulus of elasticity of the specimen is found by calculating the "weighed average" of the moduli of elasticity of fiber and matrix via the rule of mixtures:

$$E = \frac{V_{\text{f}}E_{\text{f}} + V_{\text{m}}E_{\text{m}}}{V_{\text{f}} + V_{\text{m}}}. \quad (10)$$

Using Eq. 8 with using the material properties given in the experimental section of this article, bending displacement was calculated to be $u_{\text{b}} = 548$ nm. A Poisson's ratio of 0.22 was chosen based on the values reported in the literature [26].

The penetration depth at the debonding load is calculated from Eqs. 3 and 4, which involve two unknown parameters: the penetration depth and the contact radius (u_{ep} and r_{c}). Since the two equations are linearly independent, their simultaneous solution explicitly determines the two unknowns. The penetration depth at the debonding load is $u_{\text{ep}} = 494$ nm. It should be noted that, for the same load, Fig. 4 shows a displacement of about 1,300 nm (point B), which is almost thrice the calculated penetration depth. The discrepancy between the calculated penetration depth and the measured displacement is expected, since the total displacement includes the displacement of the fiber surface due to the elastic compression of the fiber into the matrix (u_{c}), the frictional sliding of the debonded part of the fiber (u_{s}), and the deflection of the matrix due to specimen bending (u_{b}).

The elastic compression of the fiber at the start of debonding is found to be $u_{\text{c}} = 148$ nm using Eqs. 6 and 7. Similarly, using Eq. 8, bending displacement is found to be $u_{\text{b}} = 548$ nm.

Total displacement of the indenter head at the start of debonding is $u_{\text{c}} + u_{\text{b}} + u_{\text{ep}} = 1{,}190$ nm. Considering that initial displacement is not exactly zero but varies between

20 and 120 nm (see point A in Fig. 4), the total measured displacement of 1,300 nm is well justified.

The distance between points B and C represents the sliding displacement of the debonded fiber (Fig. 4). In the experiments, the fiber was pushed out about 3,000 nm before the indenter cone contacted the matrix. From the geometry of the indenter, the distance between the tip of the indenter and the point where it contacts the matrix (when the contact radius is equal to the fiber radius) can be easily calculated using

$$u_{\text{rel}} = \cot(\psi)(a - r_{\text{i}}) \tag{11}$$

where ψ is the half-included angle of the truncated cone, and a and r_{i} are the radii of the fiber and the indenter tip, respectively. For the setup described in this article, u_{rel} is found to be 2,477 nm and the sliding displacement is calculated by subtracting the penetration depth from u_{rel}:

$$u_{\text{s}} = u_{\text{rel}} - u_{\text{ep}} = 2,971\,nm \tag{12}$$

which is in very good agreement with the sliding distance observed in the tests.

The analysis of the indentation data after complete debonding (point C) is not required for calculating the IFSS. After point C, the load increases again as the matrix is indented until the maximum load is reached at point C. The reduction in slope can be attributed to the fact that, after point C the indenter is in contact with both the fiber and the matrix.

The load needed to start debonding is inversely proportional to the length of the fiber. After debonding starts, the stress transfer to the bonded part will be reduced and only the interfacial frictional stresses will act on the fiber/matrix interface. The critical length of the fiber, below which the complete debonding occurs before pullout, can be calculated using $L_{\text{c}} = a(\sigma_{\text{f}}/\tau)$, where σ_{f} is the tensile strength of the fiber and τ is the interfacial bond strength [27, 28]. According to the published data [29–32], the tensile strength of commercial carbon fibers ranges between 1.9 and 4.4 GPa. Using the average bond strength of 14.3 MPa observed in the experiments, the critical length is calculated to be in the range of 590–1,360 μm. Since the length of the fiber is about 200 μm, complete debonding before pullout is ensured. The sudden jump from B to C confirms the expected failure mode reported by Bartos [19], who has shown that the rate of debond crack propagation is inversely proportional to the fiber length and for very short fiber lengths, the debonding is complete and instantaneous.

In spite of the assumptions involved in calculating the IFSS, it is observed that the recorded nanoindentation data agree well with the analytical predictions. In Eq. 1, it was assumed that the shear stress is uniformly distributed on the interface and the effects of radial stresses were ignored. The equilibrium condition suggests that the shear stress is maximum at the top and minimum at the bottom. On the other hand, Poisson's expansion of the fiber tends to increase the strength of the fiber/matrix interface where the load is applied, thereby reducing the effect of shear-stress variation along the length of the fiber. Moreover, the bending moment generated by the load creates tensile stresses at the bottom and compressive stresses at the top, favoring crack initiation and progression, while reducing the effect of the friction forces, which depends on the friction coefficient and the magnitude of the radial stresses. The fact that there is no stress drop when debonding starts, and that the load is constant during push-out, confirms that ignoring the above-mentioned effects is acceptable for the purpose of calculating the IFSS for the experiments described here.

Conclusions

In this article, a procedure was presented for evaluating the interfacial properties of a C/C composite through microstructure characterization, push-out testing, and analytical validation. The IFSS was calculated with the assumption that the shear stress distribution is uniform on the interface, and the effects of the radial stresses are negligible. The physical soundness of these assumptions was justified by considering the mechanics of the indentation problem and identifying the components contributing to the measured displacement. It was concluded that the approach described in this article can be used in the characterization of the interfacial shear strength of C/C composites.

Acknowledgements This research was sponsored by National Science Foundation (Grant EEC 3369523372), State of Illinois and consortium of 11 industrial partners of Center for Advanced Friction Studies (http://www.frictioncenter.engr.siu.edu). The high-resolution TEM characterization was carried out at the Center for Microanalysis of Materials, University of Illinois, which is partially supported by the US Department of Energy under grant DEFG02-91-ER45439. The authors also acknowledge the contribution of Micro-imaging and Analysis Center at Southern Illinois University for assisting with the microscopy studies.

References

1. Fitzer E, Manocha LM (1998) Carbon reinforcements and carbon/carbon composites. Springer-Verlag, New York
2. Ozcan S, Filip P (2005) Wear 259:642
3. Schmidt DL, Davidson KE, Theibert LS (1999) SAMPE J 35:51
4. Cao HC, Bischoff E, Sbaizero O, Ruhle M, Evans AG (1990) J Am Ceram Soc 73:1691
5. Christin F (2005) Int J Appl Ceram Technol 2:97
6. Rice RW, Spann JR (1984) Ceram Eng Sci Proc 5:614 (ISSN 0196-6219)

7. Thouless MD, Sbaizero O, Sigl LS, Evans AG (1989) J Am Ceram Soc 72:525
8. Weins TP (1991) J Am Ceram Soc 74:535
9. Hutton TJ, Johnson D, McEnaney B (2001) Wear 249:647
10. Bradshaw WG, Vidoz AE (1978) Am Ceram Soc Bull 57:193
11. Dillon F, Thomas KM, Marsh H (1993) Carbon (UK) 31:1337
12. Manocha JM, Bahi OP, Singh YK (1989) Carbon 27:381
13. Kuntz M, Grathwohl G (2001) Adv Eng Mater (Germany) 3:371
14. Evans AG, Marshall DB (1990) Fiber reinforced ceramic composites: materials, processing and technology, vol 1. Noyes Publications, USA
15. Naslain RR (2005) Int J Appl Ceram Technol 2:75
16. Oliver WC, Pharr GM (1992) J Mater Res 7:1564
17. Li X, Bhushan B (2002) Mater Charact 48:11
18. Wittmer DE, Ozcan S, Krkoska M, Filip P (2007) Ceram Eng Sci Proc 27:665
19. Bartos P (1980) J Mater Sci 15:3122
20. Briscoe BJ, Sebastian KS, Adams MJ (1994) J Phys D: Appl Phys 27:1156
21. Zidi M, Carpentier L, Chateauminois A, Kapsa P, Sidoro F (2001) Compos Sci Technol 61(3):375
22. Nairn JA, Wagner HD (1996) Adv Comp Letts 5:131
23. Rhyne EP, Hellmann JR, Galbraith JM, Koss DA (1995) Scr Metall Mater 32(4):547
24. Mettler E, Flugge W (1962) Handbook of engineering mechanics. McGraw-Hill, New York
25. Boresi AP, Schmidt RJ (1993) Advanced mechanics of materials. Wiley, New York
26. Weeton JW, Peters DM, Thomas KL (1987) American society for metals. ASM International
27. Petersen RC (2005) J Dent Res 84(4):365
28. Chawla KK (2003) Ceramic matrix composites. Springer, USA
29. Chung DDL (1994) Carbon fiber composites. Butterworth-Heinemann, London
30. Donnet JB (1998) Carbon fibers. Marcel Dekker, New York
31. Ko TH, Ting HY, Lin CH (1988) J Appl Polym Sci 35(3):631
32. Chand S (2000) J Mater Sci 35(6):1303